

## Article

# Multiplicative Improved Coherence Factor Delay Multiply and Sum Algorithm for Clutter Removal in a Microwave Breast Tumor Imaging System

Donghao Guo <sup>†</sup>, Jingjing Wang <sup>\*,†</sup> , Huanqing Liu, Yuxi Bai, Yongcheng Li  and Weihao Liu

School of Physics and Electronics, Shandong Normal University, Jinan 250358, China; 2021020633@stu.sdnu.edu.cn (D.G.); 2021317028@stu.sdnu.edu.cn (H.L.); 2021317004@stu.sdnu.edu.cn (Y.B.); 2022020644@stu.sdnu.edu.cn (Y.L.); 2021020567@stu.sdnu.edu.cn (W.L.)

\* Correspondence: wjj@sdnu.edu.cn

<sup>†</sup> These authors contributed equally to this work.

**Abstract:** In the medical field, microwave imaging technology has experienced rapid development due to its non-invasive and non-radioactive nature. The confocal algorithm is a method commonly used for microwave breast cancer imaging, with the key objective of removing clutter in images to achieve high-quality results. However, the current methods are facing challenges in removing clutter. In order to reduce the clutter in images, a multiplicative improved coherence factor delay multiply and sum algorithm based on the maximum interclass differencing method is proposed. The algorithm compares the starting and ending moments of tumor signals in different channels to determine whether the tumor-scattered signals in different channels overlap in time. An improved coherence coefficient is obtained by summing the non-overlapping signals and multiplying the time window. The multiplicative improved coherence factor, which is obtained by multiplying the coherence coefficients of the improved multi-pair signals, is then multiplied by the focal point intensity obtained using the delay multiply and sum algorithm to reduce clutter in an image. To evaluate the performance of the proposed algorithm, several low-cost uniform and non-uniform models of human breast and tumor tissue with dielectric properties were prepared for testing. The experimental results show that, compared to the existing algorithm, the proposed algorithm can greatly reduce the clutter in images, with a signal-to-clutter ratio of at least 4 dB higher as well as contrast at least six-fold higher.

**Keywords:** breast cancer detection; confocal imaging; electromagnetic microwave imaging (EMI); CF-DAS algorithm



**Citation:** Guo, D.; Wang, J.; Liu, H.; Bai, Y.; Li, Y.; Liu, W. Multiplicative Improved Coherence Factor Delay Multiply and Sum Algorithm for Clutter Removal in a Microwave Breast Tumor Imaging System. *Appl. Sci.* **2024**, *14*, 3820. <https://doi.org/10.3390/app14093820>

Academic Editor: Vladislav Toronov

Received: 9 February 2024

Revised: 22 April 2024

Accepted: 24 April 2024

Published: 30 April 2024



**Copyright:** © 2024 by the authors. Licensee MDPI, Basel, Switzerland. This article is an open access article distributed under the terms and conditions of the Creative Commons Attribution (CC BY) license (<https://creativecommons.org/licenses/by/4.0/>).

## 1. Introduction

Breast cancer is one of various threats to women's health today, and breast screening plays a vital role in detecting cancerous tumors and thereby improving women's survival rates [1]. Currently, the primary techniques for early breast tumor detection are X-ray and magnetic resonance imaging (MRI) [2]. However, X-ray imaging has limitations due to the dense nature of breast tissue, leading to misdiagnosis rates as high as 10% to 30%. Additionally, it can cause damage to human cells through ionizing triggers, and compression of the breasts during X-ray detection can be painful for the patient [3]. Compared to X-ray imaging, MRI offers high resolution and greater accuracy in tumor detection. However, it is expensive and not easily accessible, limiting its widespread application in detection [4]. Electromagnetic microwave imaging (EMI) is an emerging and promising technique with numerous advantages for early breast tumor detection, including safety, low cost, non-ionization, and portability [5]. Several teams have reported the feasibility of their systems developed for microwave breast tumor imaging [6]. EMI can be performed using ultra-wideband (UWB) microwave imaging approaches and narrowband

approaches (microwave tomography) [7]. In microwave tomography, a profile of breast electrical properties is recovered from measurements using near-field tomographic image reconstruction algorithms. However, a requirement for microwave tomography is to solve complex inverse scattering problems, which is dependent on numerical analysis methods that are computationally intensive and slow when applied in imaging [8]. Confocal microwave imaging (CMI) is an algorithm commonly used for detecting breast cancer using UWB microwave imaging [9,10]. When a UWB microwave signal wave is directed toward breast tissues, the tissue properties, such as the dielectric constant and conductivity, cause different tissues to reflect the scattered wave signal at their boundaries. These scattered signals are acquired and used by the CMI algorithm for reconstructing images [6]. CMI does not depend on reconstruction of the media distribution within the entire imaging area and only on localizing anomalies such as tumors. In this way, the complicated inverse scattering equation is avoided, and, thus, calculation is simple and imaging rapid [11]. The delay and sum (DAS) algorithm is simple to implement and is one of the most basic and commonly used imaging algorithms in CMI [12,13]. However, the DAS algorithm yields images of poorer quality with more clutter [14]. Clutter around the tumor may mask the presence of multiple other tumors near the investigated tumor, and high-intensity clutter may be misidentified as a tumor [7]. Therefore, reducing the clutter in images is important in CMI.

The delay multiply and sum (DMAS) algorithm [7], the coherence factor delay and sum (CF-DAS) algorithm [15], and the coherence factor delay multiply and sum (CF-DMAS) algorithm [16] have been proposed to enhance image quality. The DMAS algorithm introduces a paired multiplication method based on the DAS algorithm, where the signals from different channels at each focal point are multiplied in pairs after a reverse time delay and then summed to obtain the intensity of each focal point [17]. However, after the time delay, at certain focal points where there is no tumor, the peaks of the signals from different channels are aligned with the peaks and the troughs with the troughs. After pairwise multiplication and summation by the DMAS algorithm, the intensity of the focal point is high and, therefore, generates clutter on the image. The CF-DAS and CF-DMAS algorithms use an adaptive weighting technique [18], introducing a coherence factor (CF) [19] that reflects the degree of focusing of the signal and using it to weight the intensity values at each focal point in the image [20,21]. This weighting ensures that intensity values of focus points with high CF are preserved while suppressing the intensity of focus points with low CF. However, it is important to note that at some focal points where tumors are not present, the scattered signals from tumors in different channels do not overlap in time after reverse time delays. The signal intensity cannot be canceled by summing, resulting in a high CF value. In addition, in some focal points without tumors, the signal of certain different channels are aligned peak-to-peak and valley-to-valley, with high coherence between the signals, and the signal intensity after summing and the CF value are high. After CF weighting, the intensity of a focal point without a tumor is retained, which can cause clutter in the image.

To further reduce clutter in the image, in this study, a microwave breast tumor detection system was designed that uses a multiplicative improved coherence factor delay multiply and sum (MICF-DMAS) algorithm based on the maximum interclass difference method (OTSU) algorithm [22,23]. OTSU is a nonparametric unsupervised adaptive image segmentation method in which an image is segmented into different regions by identifying the appropriate threshold value, through statistical analysis, for minimizing the variance of intensity values in the same region and maximizing the variance in different regions [24]. In this paper, first, the OTSU algorithm is used to distinguish between the scattering signals of tumors and other signals in the obtained signals, and the starting and ending moments of the tumor scattering signals for each channel are then identified to find pairs of tumor scattering signals that did not overlap in time for different channels. The absolute value of the signal intensity is taken as the gray value of the image, and the OTSU algorithm is used to obtain the optimal threshold to divide the signal into two parts with different

intensity. The first local minimum to the left of the first point in the signal that exceeds the threshold is used as the starting moment of the tumor signal. The first local minimum to the right of the last point in the signal that exceeds the threshold is taken as the moment of termination of the tumor signal. The temporal overlap between tumor scattering signals from different channels is calculated by comparing the start and stop moments of tumor signals from different channels. Since the tumor-scattered signals in the signal pairs do not overlap in time, the coherence from summing the signal pairs is higher and, hence, the CF value of the signal pairs is also higher. For pairs of signals with non-overlapping tumor scattering signals, we take the start and end time of the tumor signal received by one of the channels as the start and end time of the time window and multiply the summed signal with the corresponding element of the time window. The values of the signals inside the window remain constant, and the values of the signals outside the window become 0. This reduces the coherence sum of the signal pairs and results in a lower improved coherence factor (ICF). Then, the ICF of several signal pairs is multiplied to obtain the MICF. At some focal points where tumors are not present, some of the channels have high signal coherence and high ICF, while others have low signal coherence and low ICF. The total MICF is multiplied by a small ICF for each occurrence of a signal pair with low coherence, which reduces the MICF in focal points without tumors. In this study, we applied the proposed algorithm to a fabricated tumor model, which was imaged using the imaging system described in Section 3. By comparing with the results obtained using the DMAS, CF-DAS, and CF-DMAS algorithms on the same data, it is demonstrated that the MICF-DMAS algorithm performs better in removing image clutter, with the SCR improved by at least 4 dB and the contrast improved at least six-fold. The images obtained using the MICF-DMAS algorithm have the least amount of clutter, and MICF-DMAS can clearly distinguish the location of the tumor by reducing the influence of clutter on tumor determination.

The rest of the paper is structured as follows: The proposed MICF-DMAS algorithm is introduced in Section 2. Section 3 describes the imaging system and the experimental setup, and the proposed method is evaluated based on the experimental results. Finally, the concluding remarks are presented in Section 4.

## 2. Methods

The microwave breast tumor detection system proposed in this paper, shown in Figure 1, can be divided into three steps: signal acquisition, pre-artifact removal, and MICF-DMAS imaging to obtain the image map from the preprocessed signal:

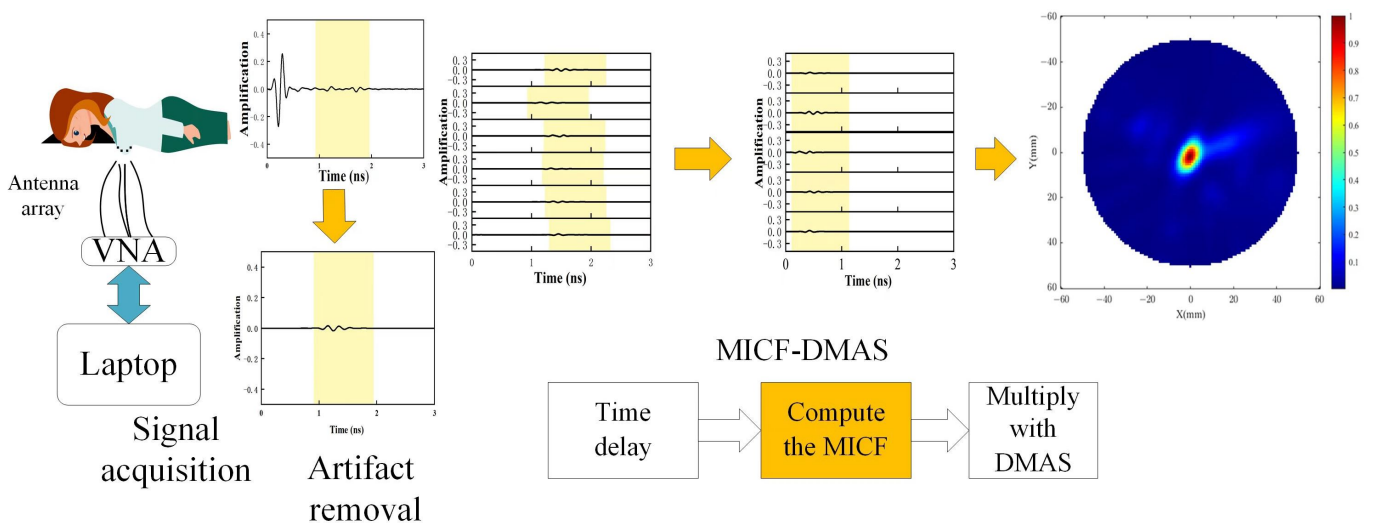


Figure 1. Microwave breast tumor detection system.

The MICF-DMAS algorithm consists of three steps: time delay, computing the MICF, and multiplying the MICF using the DMAS. First, the distance of the signal from the

transmitting antenna to the focal point of the imaging region and then to the receiving antenna is calculated and converted to a time delay. The tumor-scattered signals from all channels are reverse-delayed and synthesized to focus on a specific focal point of the imaging region within the breast. In the second step, the ICF of each focal point in the imaging region is calculated, and multiple ICF values are multiplied to obtain the MICF. The ICF indicates the coherence between signals, with a higher ICF indicating a higher coherence between signals. Detecting the start and stop moments of tumor signals in different channels allows identifying pairs of tumor scattering signals without time overlap and pairs of signals with tumor scattering signals occurring with time overlap in different channels. For pairs of tumor scattering signals that do not overlap in time in different channels, the start and stop times of the tumor signals in either channel are used as the boundaries of the time window. The signal pairs are then summed and multiplied by the time window to obtain the ICF. After this, the ICFs of multiple pairs of signals are multiplied to obtain the MICF. At the tumor focal point, the coherence between signals is higher, and multiple ICFs of higher values are multiplied. At other focal points, the MICF is multiplied by one small ICF for each signal pair with low coherence. The MICF has the advantage of amplifying the weight difference between the tumor focal point and the other focal points. Finally, the MICF is multiplied by the focal point intensity calculated using the DMAS algorithm. This reduces the intensity of the less coherent clutter focal points in the image and maintains the intensity of the more coherent tumor focal points.

### 2.1. Time Delay

Generally, antennas with very high return loss are ideal for detecting weak reflected signals. In the signals received by the antenna, the energy of the skin-reflected signal is about 90 dB higher than that of the tumor signal. The use of antenna arrays in a system often results in antenna-coupling effects [25,26]. In this study, these antenna couplings and skin-reflected signals are referred to as pre-artifacts. In this paper, a distance compensation-based dual adaptive artifact removal (DCAF) algorithm was used to remove pre-artifacts. In the DCAF algorithm, the reflection coefficients received by the antenna are first converted to the time domain using discrete inverse Fourier transform [27]. The attenuation effect due to electromagnetic wave propagation is then compensated for, and the temporal entropy threshold of the grouped signals is adaptively selected. Finally, the signals are fed into an adaptive filter with variable filter parameters to reduce the artifacts prior to imaging [28]. After removing the artifacts, the signal received by antenna  $\vec{q}_j$  transmitting  $\vec{q}_i$  after pre-artifact removal is set to  $s_{i,j}(n)$ , where  $i$  and  $j$  are the antenna index and  $n$  denotes the time series. The position of the antenna is given by  $\vec{q}_0, \dots, \vec{q}_i, \dots, \vec{q}_{N-1}$ , where  $N$  indicates the number of antennas. The block diagram of the MICF-DMAS algorithm can be seen in Figure 2. The processed tumor signals are inversely delayed and focused to each focal point of the breast. The time for propagation of the scattered signal through the breast is obtained by calculating the path from the transmitting antenna to the scattering point and to the receiving antenna [14]. The time delay  $\gamma_{i,j,e}$  from the transmitting antenna  $\vec{q}_i$  to the focal point  $\vec{m}_e$  in the imaging region to the receiving antenna  $\vec{q}_j$  is [29]

$$\gamma_{i,j,e} = \frac{(\|\vec{q}_i - \vec{m}_e\| + \|\vec{q}_j - \vec{m}_e\|)}{v}, \quad (1)$$

where  $\|\vec{q}_i + \vec{m}_e\|$  represents the propagation distance of the signal from the transmitting antenna to the focal point  $\vec{m}_e$ , where  $\|\vec{q}_j - \vec{m}_e\|$  represents the propagation distance of the signal from the receiving antenna to the focal point  $\vec{m}_e$ , and where  $e$  denotes the index of the focal point in the imaging region;  $v = c/\sqrt{\epsilon}$  is the speed of propagation of an

electromagnetic wave in a breast, and  $\epsilon$  is the dielectric constant of normal breast tissue. The signal after the time delay is denoted as

$$s_{i,j,e}(n) = s_{i,j}(n + \gamma_{i,j,e}). \tag{2}$$

If the presence of multiple reflections and the additional propagation delay caused by the denser organization inside the phantom are not taken into account [30], the signals have the same phase at focal points where scatterers are present, with the best focusing quality between the signals. The signals at locations other than the focal points where scatterers are present have poorer focusing quality [29].

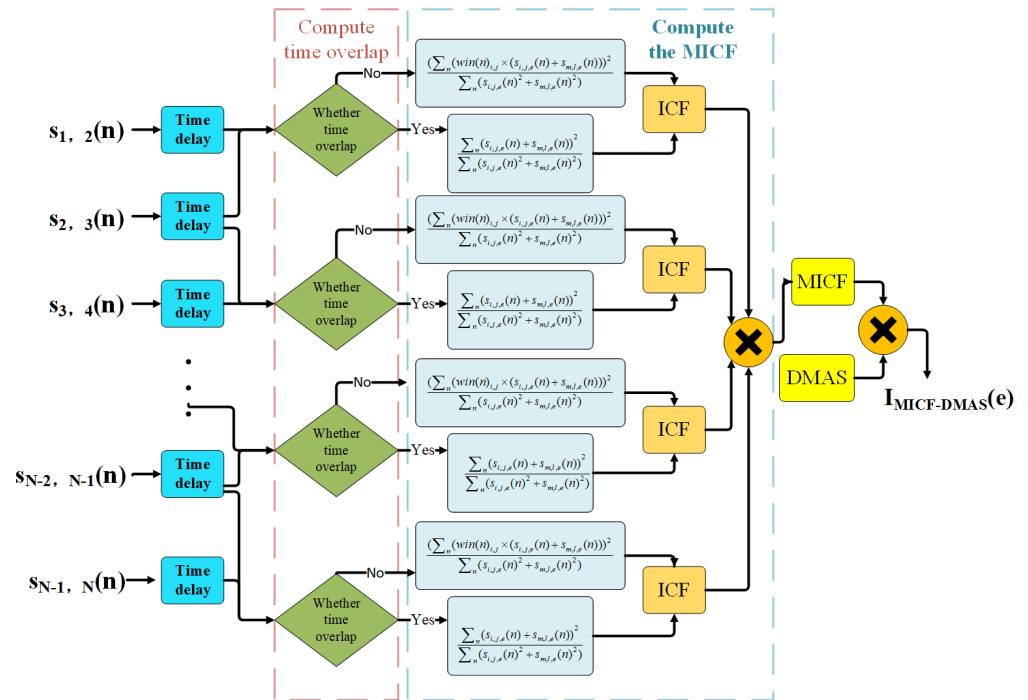


**Figure 2.** Block diagram of the MICF-DMAS algorithm for reconstructing the image of position  $\vec{m}_e$  in the breast phantom.

2.2. Computation of MICF Using Adaptive OTSU Algorithm

The clutter in images is reduced by utilizing the CF for weighting the focal point intensities [30]. The CF is calculated as follows:

$$CF_e = \frac{(\sum_n \sum_{i,j} s_{i,j,e}(n))^2}{\sum_n \sum_{i,j} (s_{i,j,e}(n))^2} \tag{3}$$

where  $(\sum_n \sum_{i,j} s_{i,j,e}(n))^2$  denotes the square of the coherent sum between the signals of different channels, and  $\sum_n \sum_{i,j} (s_{i,j,e}(n))^2$  denotes the incoherent sum between the signals of different channels. As shown in Figure 3a, the CF values between the signals are highest at the focal point where the tumor appears, and the time-delayed signals are aligned peak-to-peak and valley-to-valley. Multiplying with a high CF value preserves the intensity value of the tumor focal point. At some focal points without tumors, the time-delayed signal peaks and valleys are not aligned, as shown in Figure 3b, and the peaks and valleys cancel out after the signals are summed, so the coherent sum is lower and the CF is lower. Multiplying with a low CF reduces the intensity value of the tumor focal point. However, in some focal points without tumors, such as S16 and S23 in Figure 3c, there is no temporal overlap between the tumor scattering signals to offset the signal intensities by summation, and the higher values of the coherent sum result in higher values of CF. There is another

case, in which the focal point has no tumor and the peaks and valleys of some of the signals are aligned after a time delay, such as for S16, S23, and S37 in Figure 3d, where higher CF values are also produced. In both cases, the higher CF value multiplied by the focus intensity results in a higher intensity at the focal point where there is no tumor, creating clutter on the image.

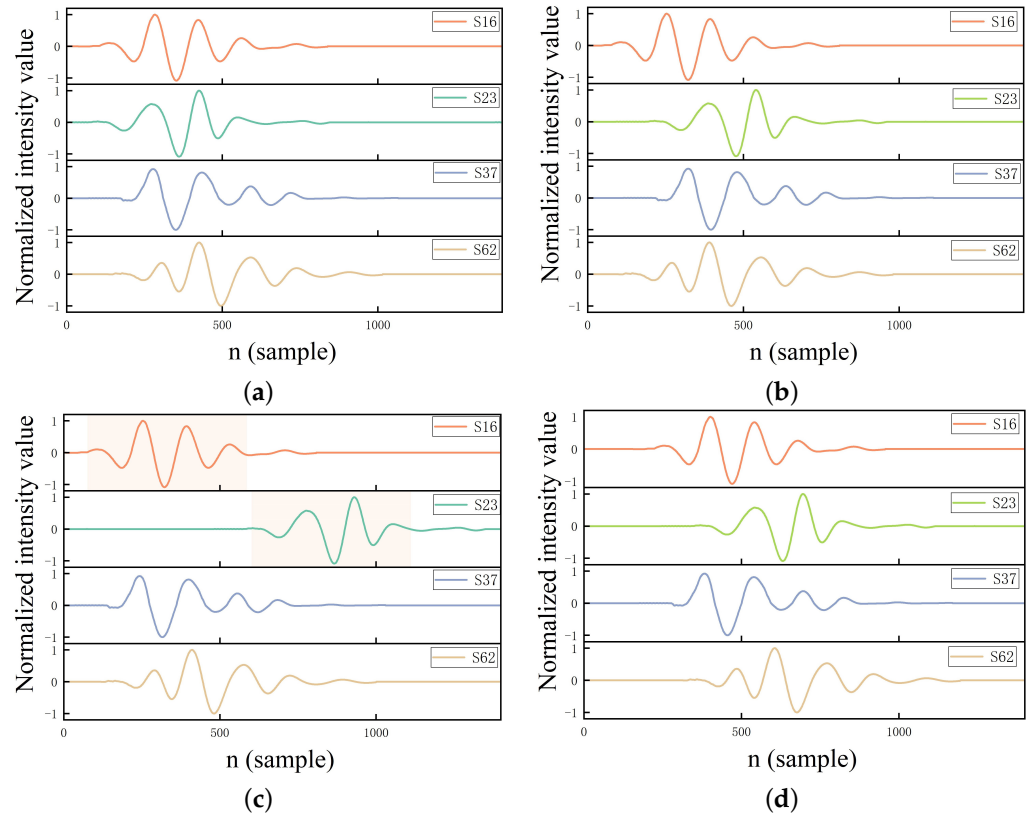


**Figure 3.** Schematic diagrams of S16, S23, S37, and S62 waveforms with different focal points. The signal strength is normalized for ease of observation: (a) Focal point of tumor presence. High coherence of different channel waveforms. (b) No tumor focal point. Low coherence of different channel waveforms. (c) No tumor focal point. Low coherence of different channel waveforms. S16 and S23 do not overlap in time. The coherent sum of S16 and S23 is high. (d) No tumor focal point. S16, S23, and S37 have high coherence.

The first step of the MICF is to find pairs of tumor signals for which there exists a temporal non-overlap. Following pre-artifact removal, signal  $s_{i,j,e}(n)$  contains high-intensity tumor scattering signals and other low-intensity residual signals. In this paper, the absolute values of the signal  $s_{i,j,e}(n)$  were represented as a grayscale histogram, the OTSU algorithm [23] was used to adaptively select the appropriate threshold value, and the signal was divided into the tumor signal region and other regions according to the intensity strength. In order to maintain the integrity of the tumor signal, the first local minimum before the first point in the signal that exceeds the threshold (point  $n_1$  in Figure 4) is used as the starting moment of the tumor signal. The first local minimum after the last point in the signal that exceeds the threshold (point  $n_2$  in Figure 4) is taken as the moment of termination of the tumor signal. By comparing the tumor signal regions across different channels, we determine whether there is a temporal overlap of tumor signals. We assume that the start and end times of the tumor signal region in signal  $s_{i,j,e}(n)$  are  $n_{i,j,e,start}$  and  $n_{i,j,e,stop}$ . We assume that the intensity values of signal  $|s_{i,j,e}(n)|$  range from  $[A_{min}, A_{max}]$ .  $A_f$  is one of the intensity values in signal  $|s_{i,j,e}(n)|$ . The number of points with intensity value  $A_f$  in signal  $|s_{i,j,e}(n)|$  is  $e_f$ . The total number of points of the discrete signal  $|s_{i,j,e}(n)|$  is  $U$ . The normalized probability of occurrence of  $A_f$  is  $b_f$ , which can be expressed as

$$b_f = \frac{e_f}{U}. \tag{4}$$

The absolute values of signal intensity are divided into two groups using the threshold  $P$ :  $C_0 \in (A_{\min}, P)$ ,  $C_1 \in (P, A_{\max})$ . The probability of each group occurring is

$$w_0 = P(C_0) = \sum_{A_f \in C_0} b_f, \tag{5}$$

$$w_1 = P(C_1) = \sum_{A_f \in C_1} b_f. \tag{6}$$

The mean value within the group is

$$\mu_0 = \sum_{A_f \in C_0} A_f \frac{b_f}{w_0}, \tag{7}$$

$$\mu_1 = \sum_{A_f \in C_1} A_f \frac{b_f}{w_1}. \tag{8}$$

The overall mean is

$$\mu_T = \sum_{A_f \in [A_{\min}, A_{\max}]} g_f b_f. \tag{9}$$

The within-group variances for the two groups are

$$\sigma_0^2 = \sum_{A_f \in C_0} (A_f - \mu_0)^2 \frac{b_f}{w_0}, \tag{10}$$

$$\sigma_1^2 = \sum_{A_f \in C_1} (A_f - \mu_1)^2 \frac{b_f}{w_1}. \tag{11}$$

The between-class variance is

$$\sigma_T^2 = w_0(\mu_0 - \mu_T)^2 + w_1(\mu_1 - \mu_T)^2. \tag{12}$$

The threshold  $P$  is a function of  $\sigma_T^2$ . The optimal threshold  $P^*$  can be determined by maximizing  $\sigma_T^2$  [23]

$$\sigma_T^2(P^*) \max_{P \in [A_{\min}, A_{\max}]} \sigma_T^2(P). \tag{13}$$

The time window in which the tumor-scattered signal exists is  $[n_{i,j,e,start}, n_{i,j,e,stop}]$ . The first local minimum before the first point in the signal that exceeds the threshold  $P^*$  is used as the starting moment  $n_{i,j,e,start}$  (point n1 in Figure 4) of the tumor signal. The first local minimum after the last point in the signal that exceeds the threshold is used as the termination moment  $n_{i,j,e,stop}$  (point n2 in Figure 4) of the tumor signal. If signals  $s_{i,j,e}(n)$  and  $s_{m,l,e}(n)$  have no time overlap, then  $n_{i,j,e,stop} < n_{m,l,e,start}$  or  $n_{i,j,e,start} < n_{m,n,e,stop}$ .

In the second step, for pairs of tumor scattering signals with no temporal overlap in different channels, the start and stop times of the tumor signals in one of the channels are used as the boundaries of the time window. The signals are summed, the corresponding element of the signal is multiplied by the corresponding element of the time window, and the coherent sum is then obtained by integrating the squares of the signals. The ICF can be expressed as

$$ICF_{ij,ml,e} = \begin{cases} \frac{(\sum_n (win(n)_{i,j} \times (s_{i,j,e}(n) + s_{m,l,e}(n))))^2}{\sum_n (s_{i,j,e}(n)^2 + s_{m,l,e}(n)^2)}, & \text{no time overlapping} \\ \frac{\sum_n (s_{i,j,e}(n) + s_{m,l,e}(n))^2}{\sum_n (s_{i,j,e}(n)^2 + s_{m,l,e}(n)^2)}, & \text{others} \end{cases} \tag{14}$$

where

$$win(n)_{i,j} = \begin{cases} 1, & (n_{i,j,e,start} < n < n_{i,j,e,stop}) \\ 0, & \text{others} \end{cases} \tag{15}$$

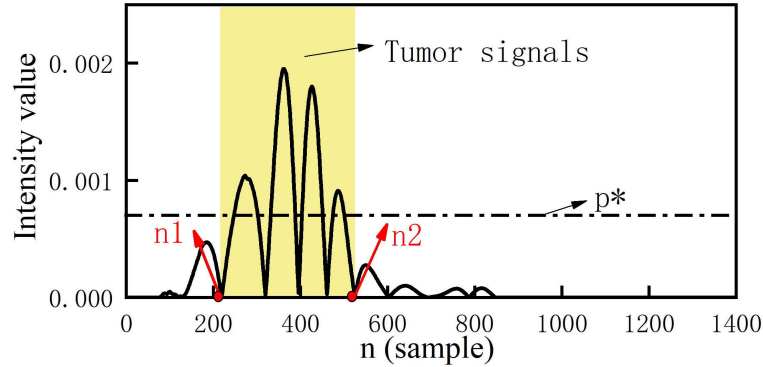


**Figure 4.** Determination of the starting and ending moments of the tumor scattering signal using the OTSU algorithm. The dashed line is the optimal threshold. The yellow shaded area is the tumor scattering signal; n1, n2 denote the start and the stop moments of the tumor signal.

Figure 5 indicates the extent of the time window. From (14), it can be seen that upon multiplying the summed signals with the time window the value of the numerator (the coherent sum of the signal pairs) is reduced, while the denominator (the incoherent sum of the signals) remains unchanged. As a result, the ICF value obtained is lower than the CF value not multiplied by the time window. The signals from the different transceiver antennas ( $s_{1,2}, s_{2,3}, s_{3,4}, \dots, s_{N-1,N}$ ) already contain all the tumor information. To minimize calculation, the total  $MICF_e$  is obtained by multiplying  $ICF_{ij,mn,e}$  of the different signals of the transceiver antennas:

$$MICF_e = \prod_{i,j,m,n} ICF_{ij,mn,e} \tag{16}$$

At a focal point where there is no tumor, the MICF of each pair of low-coherence signals is multiplied by a small factor. On the other hand, at a focal point with a tumor, the MICF is multiplied by a larger factor. Compared to the CF, the MICF shows a greater difference between the tumor focal point and the other focal points.

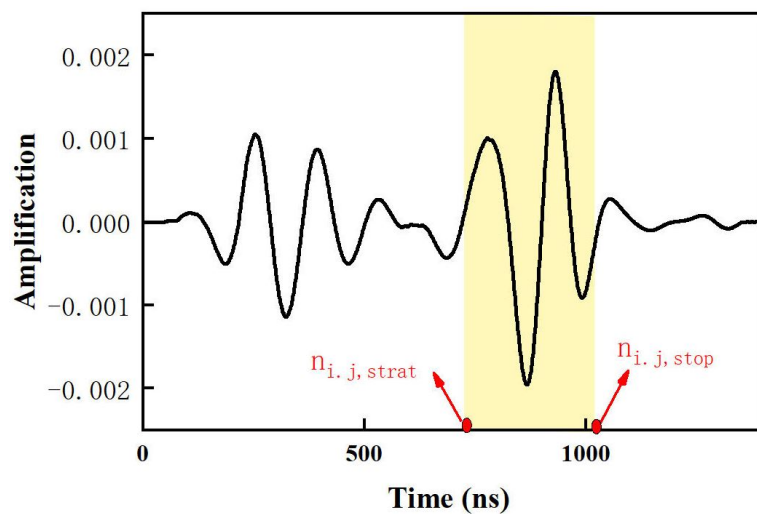


**Figure 5.** The start and end points of the window function in (15). The yellow shaded area is the range of the time window.

### 2.3. MICF Multiplied by DMAS

Finally, the MICF is multiplied by the focal point intensity value of the DMAS-derived image, and the MICF is utilized to suppress the less coherent clutter in the image, resulting in better image quality. Arranged in the order of the antennas,  $s_{i,j,e}(n)$  is denoted as  $s_{p,e}(n)$  where  $p$  is the antenna index. The synthesized wave of focus  $\vec{m}_e$  in the breast is expressed as

$$I_e = MICF_e \times \left\| \sum_p \sum_q s_{p,e}(n) \times s_{q,e}(n) \right\| (p \neq q). \quad (17)$$

The above process is repeated for each focal point in the breast to generate the energy map.

## 3. Experiment

### 3.1. Experimental Setup

In this paper, an ultra-wideband microwave breast cancer detection system was proposed for testing the proposed algorithm. As shown in Figure 6, the system consisted of six small ultra-wideband Vivaldi antennas arranged in an antenna array, a Keysight P5023B multi-port vector network analyzer (VNA) with a frequency range of 9 KHz–14 GHz, a laptop computer, and a circular plastic mount for securing the antennas. The VNA and the ultra-wideband antenna were connected via six coaxial cables to transmit and receive signals. The breast phantom was exposed to an ultra-wideband microwave signal covering the frequency band from 2.5 to 8 GHz, striking a balance between penetration depth and image resolution [31]. In this study, the number of sampling points was set to 1001, which increased the calculation workload but also expanded the scanning distance of the VNA [28]. The VNA had an output power of 10 dBm. Ultra-wideband microwave signals were sequentially transmitted from one port of the VNA through the antenna to the experimental model, while the remaining ports collected the scattered signals. The received signals were stored in a laptop, and the images were then reconstructed using the proposed MICF-DMAS algorithm.

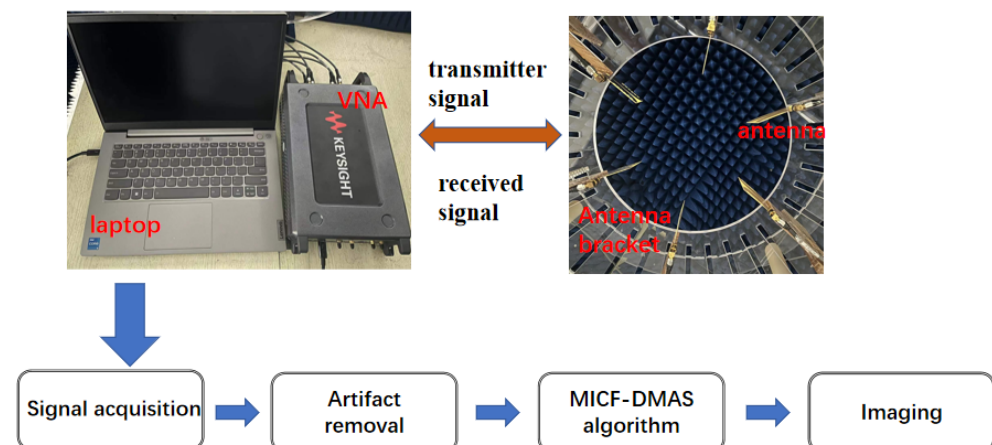


**Figure 6.** Microwave imaging system.

The system utilized a three-dimensional section of the breast, facing the center of the breast, for imaging purposes. To achieve this, a 3-D antenna array was employed in the Z-direction to scan the breast slices [25]. A circular support made of an acrylic plate with a diameter of 50 cm was used to hold six small ultra-wideband Vivaldi antennas [32] forming the antenna array. The antennas were spaced at  $60^\circ$  intervals, ensuring mutual coupling between them was less than  $-20$  dB. The center of the antenna array aligned with the center of the breast model, and each antenna was positioned 5 mm away from the outer surface of the breast model. Using such an arrangement allowed avoiding the use of high-intensity microwaves [25]. Each antenna, measuring  $45 \text{ mm} \times 40 \text{ mm} \times 1.2 \text{ mm}$  (Figure 7), was printed on a Fr4 substrate and had a bandwidth of 2.5 GHz–10 GHz. Signal

transmission was carried out sequentially, with one antenna transmitting at a time while the rest received the signal. This process was repeated until each of the six antennas had transmitted a signal.

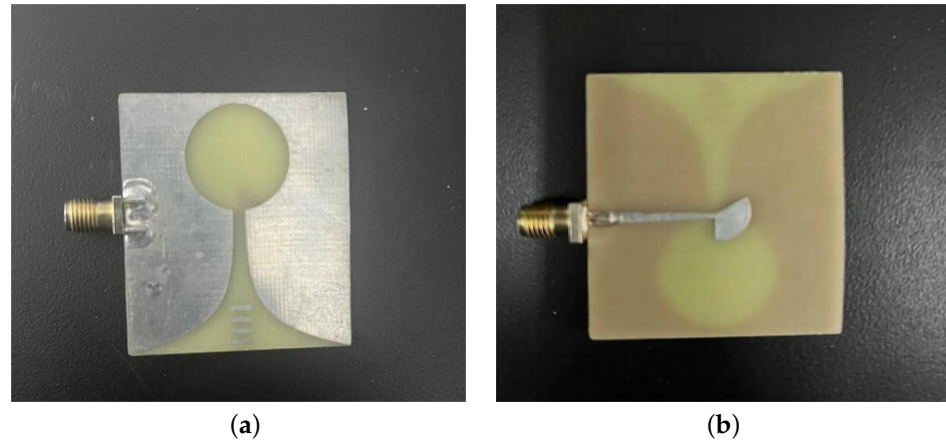


**Figure 7.** The antenna used in the imaging system: (a) Top view. (b) Bottom view.

### 3.2. Experimental Model

In this study, three realistic breast phantoms were utilized to evaluate the imaging performance of the system on breast tumors. The fabrication and measurement of each breast prosthesis was conducted following the methodology described in references [33,34]. Phantom (I) was a homogeneous phantom consisting of a single medium, as shown in Figure 8a. The materials and proportions are listed in Table 1. In homogeneous media, after a reverse time delay, the signal at the focal point where a tumor is present has higher coherence. The model consisted of a 50 mm hemisphere filled with a homogeneous medium simulating normal breast tissue. Based on the clinical investigation and analysis of patients with early breast tumors, it has been found that the diameter of breast tumors can range from 9 to 58 mm with an average diameter of 22.1 mm [35]. Additionally, it has been observed that the closer the tumor is to the skin, the higher the likelihood of lymph node metastasis, and the rehabilitation outcomes tend to be relatively poor [28]. Therefore, a cylindrical medium with a diameter of 10 mm and a thickness of 10 mm was inserted at appropriate coordinates ( $X = 17$  mm,  $Y = -23$  mm,  $Z = 45$  mm) for simulating a near-skin tumor. Phantom (II) used a three-layer skin–fat–tumor structure to simulate a heterogeneous phantom that more closely resembled a real human breast (Figure 8b). The materials and proportions are listed in Table 2. The outer surface of the model was a hemispherical hollow medium for simulating the skin layer, and the interior was filled with a hemispherical medium for simulating the fat layer. It was noted in a previous clinical study that the uneven thickness of a patient’s skin can greatly affect the detection of suspicious areas within the breast [36]. Therefore, we set the simulated skin media thickness to 9–12 mm to simulate uneven skin thickness. The phantom diameter and the tumor diameter and location were the same as for phantom (I). Phantom (III) had an additional 10 mm in tumor diameter compared to phantom (II) and was located at ( $X = -25$  mm,  $Y = 18$  mm,  $Z = 45$  mm) to simulate the case of multiple targets (Figure 8c). The presence of multiple targets can result in multiple internal reflections that may affect the imaging system.

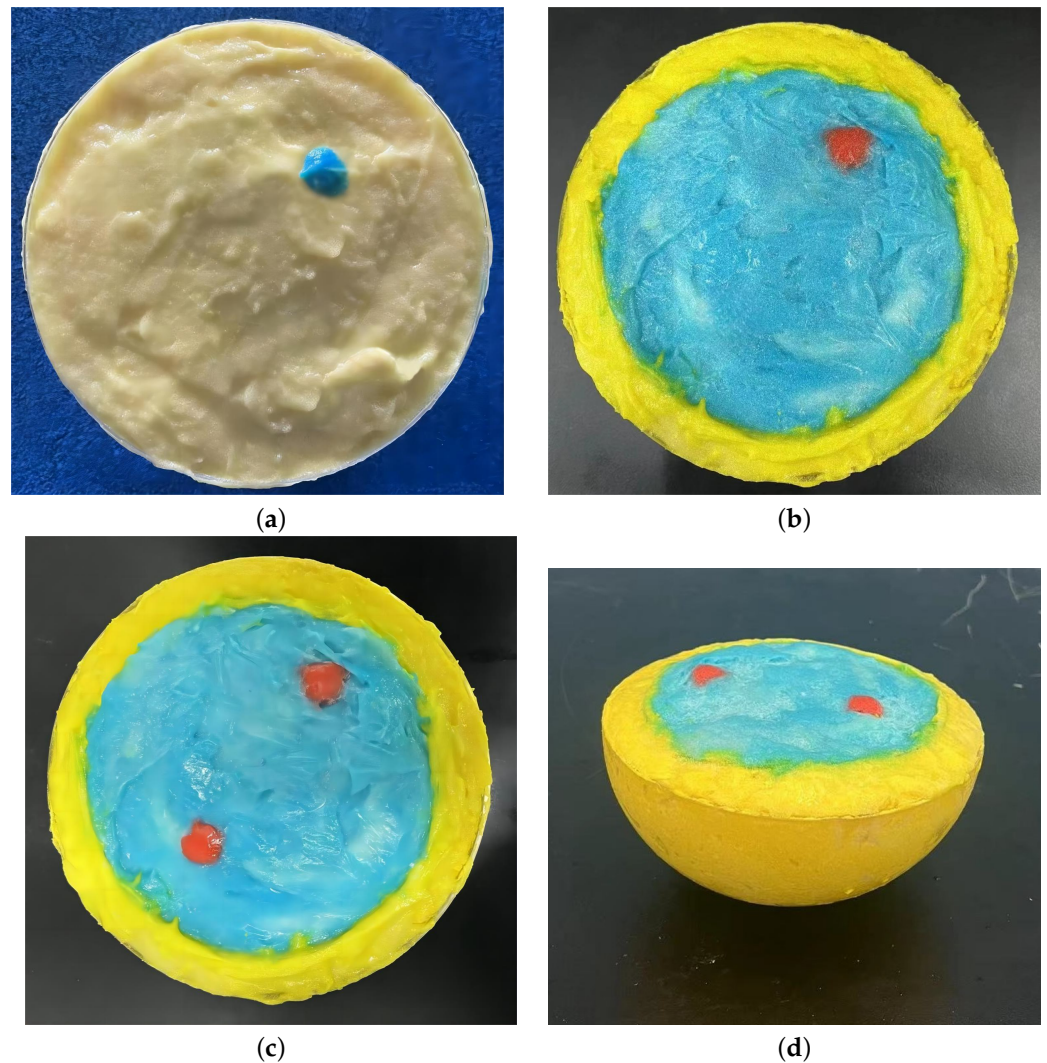


**Figure 8.** (a) Single-tumor homogeneous phantom (I). (b) Single-tumor heterogeneous phantom (II). (c) Two-tumor heterogeneous phantom (III). (d) The profile of phantom (III).

**Table 1.** Phantom (I) composition: materials and scale.

Material	Normal Tissue	Tumor	Purpose
distilled water (mL)	420	420	solvent
polyethylene powder (g)	480	430	adjusts the dielectric constant
agar (g)	20	20	maintains model shape
NaCl (g)	6.8	28.3	increases electrical conductivity
xanthan gum (g)	6.25	6.25	thickening agent
sodium dehydroacetate (g)	0.25	0.25	preservative

**Table 2.** Phantom (II) composition: materials and scale.

Material	Skin	Fat	Tumor	Purpose
distilled water (mL)	420	420	420	solvent
polyethylene powder (g)	450	500	430	adjusts the dielectric constant
agar (g)	20	20	20	maintains model shape
NaCl (g)	20	2.3	28.3	increases electrical conductivity
xanthan gum (g)	6.25	6.25	6.25	thickening agent
sodium dehydroacetate (g)	0.25	0.25	0.25	preservative

### 3.3. Evaluation Indicators

The performance of the algorithms was assessed using four metrics: contrast ratio CR; signal-to-clutter ratio SCR; the coordinate  $X$  of the point with the highest intensity value in the image; and the tumor diameter  $D$ . CR measures the ratio of the mean intensities of the tumor site to the breast tissue, while SCR compares the maximum intensities of the tumor site to the corresponding region of healthy tissue, and  $D$  is the diameter of the area within 40% of the intensity range around the highest intensity point in the image [37]. CR and SCR are denoted as

$$CR = \frac{\text{mean}(I_t)}{\text{mean}(I_b)}, \quad (18)$$

$$SCR = 10\log_{10}\left(\frac{\max(I_t)}{\max(I_b)}\right), \quad (19)$$

where  $I_t$  and  $I_b$  are the intensity of the tumor region and the intensity of other tissues. A higher value of CR indicates a greater contrast between the tumor and normal portions of the image. A higher SCR value indicates there is less clutter in the image.

### 3.4. Dielectric Constant Measurement

The imaging algorithm in this study utilizes signal time delay to achieve focused imaging. The time delay  $\gamma$  of the imaging point relative to each antenna is first calculated, then the signal is shifted using  $\gamma$ , and, finally, multiple signals are focused for imaging:

$$\gamma = \frac{d}{c/\sqrt{\epsilon}} \quad (20)$$

where  $d$  denotes the relative permittivity of the medium,  $\epsilon$  denotes the propagation distance, and  $c$  denotes the speed of light. When the signal propagates the same distance in different biological tissues, the propagation delay  $\gamma$  is related only to the dielectric constant of biological tissue, and an accurate dielectric constant will improve imaging quality [27]. The dielectric constant of the phantom was measured using a Keysight coaxial probe kit (Keysight N1501A), as shown in Figure 9. Figure 10 shows the measured and target values of the dielectric constant and conductivity relative to the frequency of tumor, skin, and fat materials. The dielectric constant and conductivity of the homogeneous phantom (I) in Figure 10a,b were identical to the target curves. Figure 10c,d show the dielectric constant and conductivity of each material (skin, fat, and tumor) in the heterogeneous phantoms (II) and (III). The values of the dielectric constants of the three substances generally decreased at different slopes as the frequency increased. Tumor had the highest value of dielectric constant, followed by skin, and fat had the lowest [34]. The data of this experimental model satisfied the experimental requirements.



Figure 9. Dielectric constant measurement.

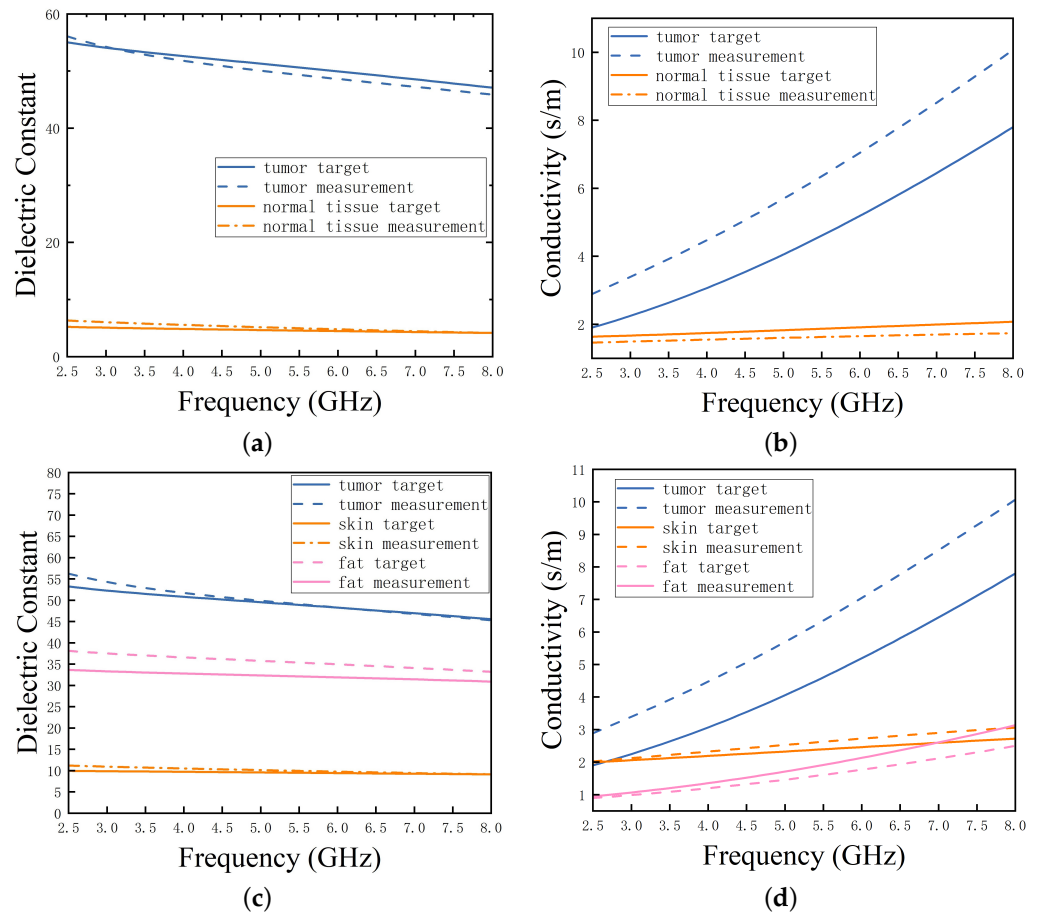


**Figure 10.** (a) Dielectric constants and (b) conductivity of tumor and normal tissue in phantom (I). (c) Dielectric constants and (d) conductivity of tumor, fat, and skin in phantoms (II) and (III).

### 3.5. Experimental Results

We used phantom (I) for imaging toward verifying that the images obtained using the MICF-DMAS algorithm on a homogeneous phantom had less clutter. Phantom (I) was a homogeneous phantom consisting of a single medium, and the tumor, measuring 10 mm in diameter, was situated at coordinates (17 mm, −23 mm). Figure 11 shows the imaging results obtained for phantom (I) using the four algorithms DMAS, CF-DAS, CF-DMAS, and MICF-DMAS. All the images were normalized based on the maximum intensity value in the reconstruction plane, with yellow representing the highest value and blue representing the lowest. The images obtained using the DMAS and CF-DAS algorithms contain more low-intensity clutter. There is reduced clutter in the image obtained by the CF-DMAS algorithm, but some clutter is still present. There is almost no clutter in the image obtained using the MICF-DMAS algorithm. Table 3 presents the SCR, CR, X, and D values. SCR and CR were used to assess the level of clutter in the image and the contrast between the tumor and normal tissue. A higher SCR value indicates reduced clutter and improved imaging clarity, while a higher CR value suggests an increased image contrast ratio. Compared with the other three algorithms, the MICF-DMAS algorithm improved the SCR by at least 4 dB and the CR at least four-fold. Similar coordinates X for the point of maximum intensity in the images were obtained using the four algorithms. D represented the diameter of the tumor. The DMAS, CF-DAS, CF-DMAS, and MICF-DMAS algorithms yielded images with D of 11.3 mm, 10.7 mm, 9.6 mm, and 8.1 mm. The diameter of the tumor obtained by the MICF-DMAS algorithm was smaller compared to the true value (10 mm). The reason is that the MICF-DMAS algorithm suppressed the intensity of the focus near the tumor.

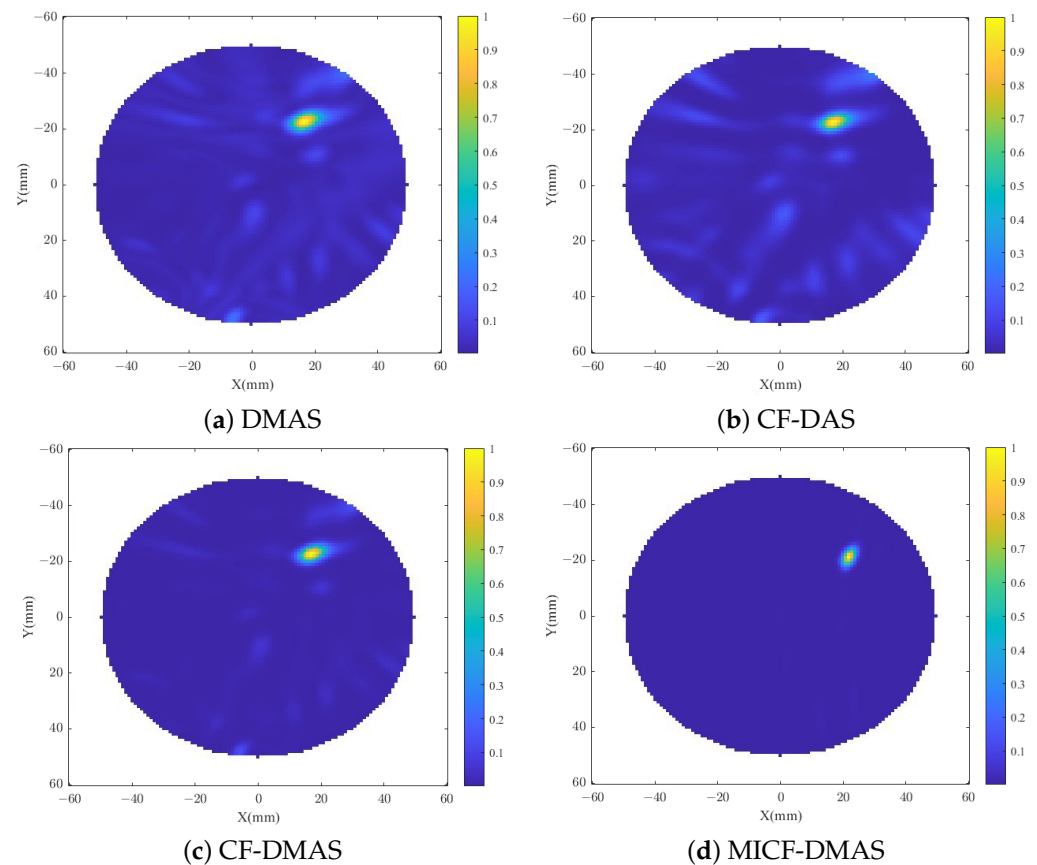


**Figure 11.** Imaging results of the four algorithms for the homogeneous single-tumor phantom (I) ( $Z = 45$  mm).

**Table 3.** Evaluation indicators of the four algorithms for the homogeneous single-tumor phantom (I) imaging results.

Method	$D$ (mm)	$X$ (mm)	SCR (dB)	CR
MICF-DMAS	8.1	(18, −25)	14.72	23.14
CF-DAS	10.7	(18, −25)	5.52	11.46
DMAS	11.3	(19, −24)	6.09	11.92
CF-DMAS	9.6	(19, −25)	10.61	17.68

We used phantom (II) for imaging toward verifying that the MICF-DMAS algorithm minimized clutter when imaging individual tumors in a heterogeneous model that more closely resembled a real breast. Phantom (II) was a non-homogeneous model consisting of three layers of skin, fat, and tumor, and the tumor, measuring 10 mm in diameter, was situated at coordinates (17 mm, −23 mm) with skin thickness of 9–12 mm. Figure 12 shows the imaging results obtained for phantom (II) using the four algorithms. Due to the inhomogeneous media and skin thickness, the images of Figure 12 show more clutter compared to those of Figure 11 in addition to a larger tumor localization error of about 6 mm. The results obtained using the DMAS and CF-DAS algorithms are depicted in Figure 12a,b, showing that the images contain a large amount of clutter. Notably, there is high-intensity clutter at coordinates (−23 mm, −20 mm) that could be mistaken for a tumor. As can be seen in Figure 12c, there is less clutter in the image obtained by the CF-DMAS algorithm, but the high-intensity clutter at (−23 mm, −20 mm) is still present. Figure 12d shows the image obtained using the MICF-DMAS algorithm, clearly showing a tumor, and the intensity and instances of clutter are reduced. The high-intensity area around the tumor is minimal. The high-intensity clutter located at (−23 mm, −20 mm) was also suppressed to a low intensity. Table 4 presents the SCR and CR of the images acquired

using the four algorithms. The MICF-DMAS algorithm has an SCR of 13.94 dB and a CR of 20.32. The SCR of the image obtained using the MICF-DMAS algorithm is about 6 dB higher than that of the images obtained using the CF-DMAS algorithm. In addition, the CR values also indicate better performance, with a higher percentage of intensity values focused on the tumor and less clutter.

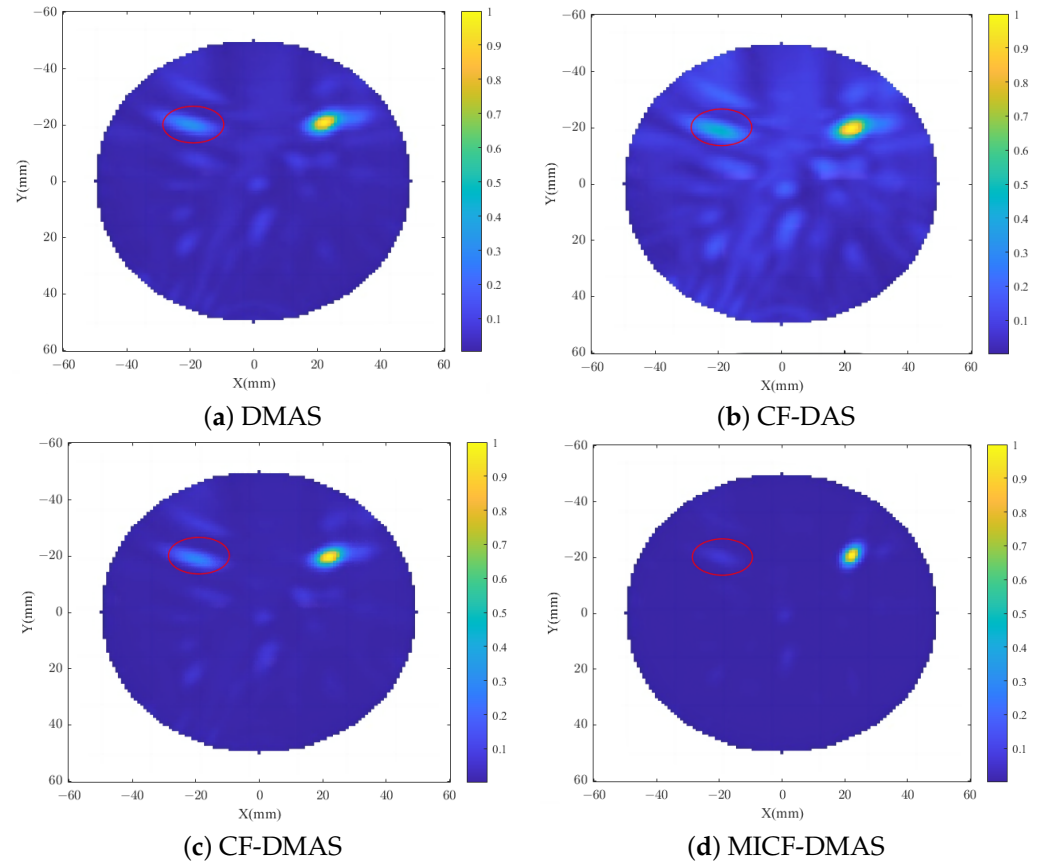


**Figure 12.** Imaging results of the four algorithms for the heterogeneous single-tumor phantom (II) ( $Z = 45$  mm). The portion circled by the red circle indicates high intensity clutter.

**Table 4.** Evaluation indicators of the four algorithms for the heterogeneous single-tumor phantom (II) imaging results.

Method	D (mm)	X (mm)	SCR (dB)	CR
MICF-DMAS	8.5	(21, −20)	13.64	21.32
CF-DAS	10.9	(22, −20)	5.03	9.41
DMAS	11.4	(21, −21)	5.36	10.39
CF-DMAS	10.2	(21, −20)	7.93	15.51

We used phantom (III) for imaging to validate the imaging performance of the MICF-DMAS algorithm for multiple targets. The tumors had a diameter of 10 mm each, with tumor 1 located at (17 mm, −23 mm) and tumor 2 located at (−25 mm, 20 mm). As shown in Figure 13, the presence of multiple targets led to multiple internal reflections, resulting in more clutter in the images obtained by the four algorithms [30]. The DMAS and CF-DAS algorithms produced images with a significant amount of high-intensity clutter. More clutter is also present in the images obtained by the CF-DMAS algorithm. More high-intensity clutter may be mistaken for tumors, which may have certain effects on tumor localization. The intensity and instances of clutter are significantly improved upon in the images obtained by the MICF-DMAS algorithm. Table 5 presents the results, indicating that the MICF-DMAS algorithm achieved the highest SCR and CR. Since there were two

tumors in phantom (III),  $X$  took the coordinates of the two points with the highest intensity of the focal points, and  $D$  also took the portion of high intensity around these two points. Similar coordinates of highest intensity for the two points were obtained within the images using the four methods, with the smallest  $D$  obtained by the MICF-DMAS algorithm and a larger  $D$  obtained using the CF-DAS and DMAS algorithms.

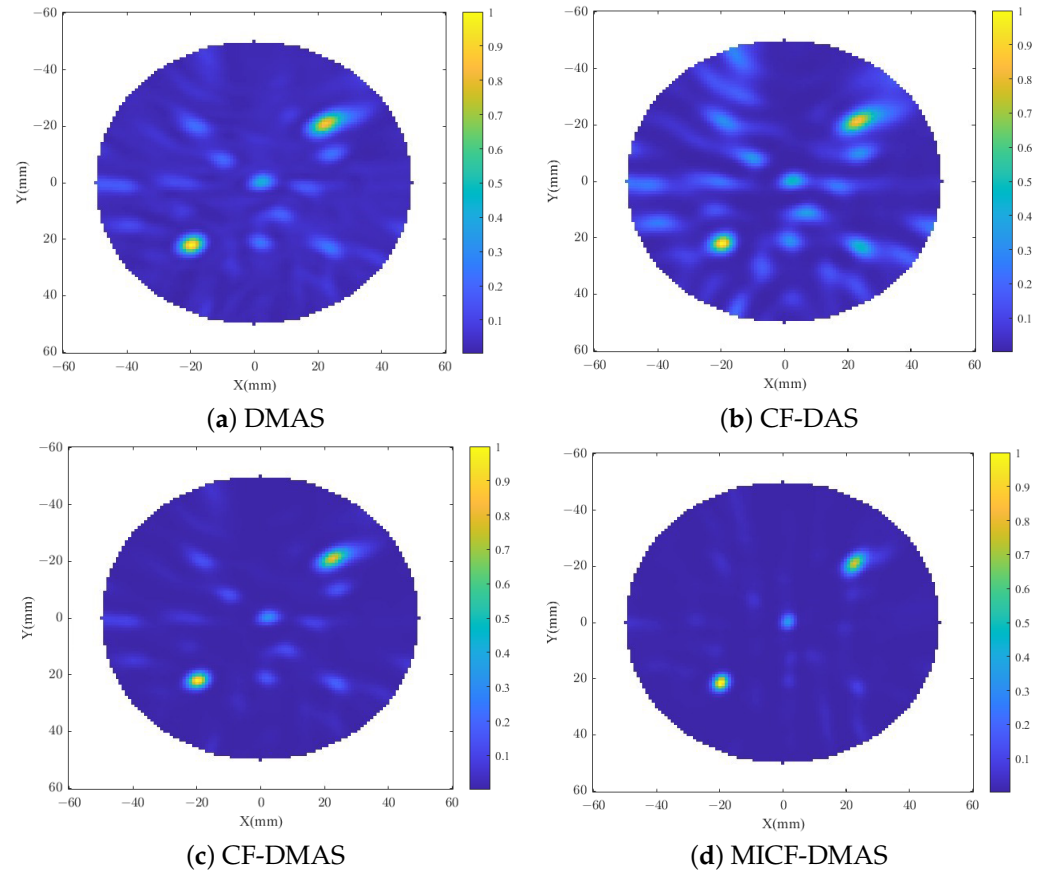


**Figure 13.** Imaging results of the four algorithms for the heterogeneous two-tumor phantom (III) ( $Z = 45$  mm).

**Table 5.** Evaluation indicators of the four algorithms for the heterogeneous two-tumor phantom (III) imaging results.

Method	MICF-DMAS	CF-DAS	DMAS	CF-DMAS
D1 (mm)	8.1	9.7	10.1	9.6
D2 (mm)	9.2	12.1	12.6	11.6
X1 (mm)	(22,−20)	(22,−20)	(21,−20)	(22,−21)
X2 (mm)	(−19,17)	(−19,18)	(−19,18)	(−19,17)
SCR (dB)	10.26	4.03	4.21	5.91
CR	19.4	10.46	10.92	18.35

### 3.6. Discussion

In some lesions without tumors and after time delay, the signals of certain channels are highly coherent, or the signals of certain channels appear at non-overlapping times. The intensity of these signals remains high after pairwise multiplication and summation by the DMAS algorithm. Therefore, the image obtained using the DMAS algorithm has more clutter, and the coherent sum of these signals is high, which leads to high CF values. As a result, the images obtained using the CF-DAS and CF-DMAS algorithms also have some clutter. The MICF-DMAS algorithm retains the coherence of the DMAS algorithm and improves upon it using MICF weighting. In MICF, an ICF of lower weight is first

obtained by adding a time window to signals that do not overlap in time. The ICF values for multiple pairs of signals are then multiplied together to obtain the MICF. For each pair of signals with low coherence in the clutter focus, the MICF is multiplied by a factor of low value, which reduces the weight of the clutter focus. Compared to the original CF, the focus points of the improved MICF have lower weights in cases of clutter. As shown in Figure 12, high-intensity clutter is exhibited at (−23 mm, −20 mm) in the images acquired using the CF-DAS and CF-DMAS algorithms but not the MICF-DMAS algorithm. As a result, the MICF-DMAS algorithm yields images with less clutter and the highest SCR and CR. The MICF-DMAS algorithm does not change the focus of the signal, so the coordinates corresponding to the highest pixel value in the image are similar to those of the other three algorithms. The MICF is obtained by multiplying multiple ICF values and is more sensitive to signal coherence. Focused signals around the highest intensity point in the image are less coherent and have smaller MICF values. The focused intensity obtained after MICF weighting is small. The MICF-DMAS algorithm yields images with the smallest diameter of the high-intensity region around the point with the highest pixel value.

#### 4. Conclusions

In this paper, we propose an MICF-DMAS algorithm based on maximum interclass difference to reduce clutter. This algorithm, which is an improvement of the original CF algorithm, can adaptively detect signal pairs without temporal overlap and add time windows to the numerator of its CF to obtain ICF values. The ICF values of multiple pairs of signals are then multiplied to reduce the weight of clutter focal points and improve the image quality. The MICF-DMAS algorithm was compared with the DMAS, CF-DAS, and CF-DMAS algorithms through multi-objective experiments. The results for the evaluation metrics show that the MICF-DMAS algorithm performs better overall than the other algorithms. It effectively removes clutter and improves the image quality, with the SCR being at least 4 dB better, and the contrast is at least six-fold higher than that of the existing algorithms. Since this research is still in the laboratory stage, some shortcomings need to be addressed. There is still room to improve the localization accuracy of the proposed method, and advanced machine learning algorithms will be utilized together with convolutional neural networks and multimodal methods in future work toward improving the accuracy of the microwave imaging system, further improving the SCR and the CR [38–40].

**Author Contributions:** D.G.: software, writing—original draft preparation. J.W.: conceptualization, methodology, writing—review and editing. H.L.: validation, resources, visualization. Y.B.: formal analysis. Y.L.: validation, data curation. W.L.: validation, project administration. All authors have read and agreed to the published version of the manuscript.

**Funding:** This research received no external funding.

**Institutional Review Board Statement:** Not applicable.

**Informed Consent Statement:** Not applicable for studies not involving humans.

**Data Availability Statement:** The data that have been used are confidential.

**Conflicts of Interest:** The authors declare no conflicts of interest

#### References

1. Sung, H.; Ferlay, J.; Siegel, R.L.; Laversanne, M.; Soerjomataram, I.; Jemal, A.; Bray, F. Global Cancer Statistics 2020: GLOBOCAN Estimates of Incidence and Mortality Worldwide for 36 Cancers in 185 Countries. *CA A Cancer J. Clin.* **2021**, *71*, 209–249. [[CrossRef](#)] [[PubMed](#)]
2. Moloney, B.M.; O’Loughlin, D.; Elwahab, S.A.; Kerin, M.J. Breast Cancer Detection—A Synopsis of Conventional Modalities and the Potential Role of Microwave Imaging. *Diagnostics* **2020**, *10*, 103. [[CrossRef](#)] [[PubMed](#)]
3. Kwon, S.; Lee, S. Instantaneous microwave imaging with time-domain measurements for breast cancer detection. *Electron. Lett.* **2013**, *49*, 639–641. [[CrossRef](#)]
4. Mahmud, M.Z.; Islam, M.T.; Misran, N.; Kibria, S.; Samsuzzaman, M. Microwave Imaging for Breast Tumor Detection Using Uniplanar AMC based CPW-fed Microstrip Antenna. *IEEE Access* **2018**, *6*, 44763–44775. [[CrossRef](#)]

5. Nguyen, D.H.; Stindl, J.; Slanina, T.; Zimmer, G. High Frequency Breast Imaging: Experimental Analysis of Tissue Phantoms. *IEEE Open J. Antennas Propag.* **2021**, *2*, 1098–1107. [[CrossRef](#)]
6. Klemm, M.; Craddock, I.J.; Leendertz, J.A.; Preece, A.; Benjamin, R. Radar-Based Breast Cancer Detection Using a Hemispherical Antenna Array—Experimental Results. *IEEE Trans. Antennas. Propag.* **2009**, *57*, 1692–1704. [[CrossRef](#)]
7. Lim, H.B.; Nhung, N.T.T.; Li, E.P.; Thang, N.D. Confocal microwave imaging for breast cancer detection: Delay-multiply-and-sum image reconstruction algorithm. *IEEE Trans. Biomed. Eng.* **2008**, *55*, 1697–1704. [[PubMed](#)]
8. Fear, E.C.; Li, X.; Hagness, S.C.; Stuchly, M.A. Confocal microwave imaging for breast cancer detection: Localization of tumors in three dimensions. *IEEE Trans. Biomed. Eng.* **2002**, *49*, 812–822. [[CrossRef](#)] [[PubMed](#)]
9. Fear, E.C.; Bourqui, J.; Curtis, C.; Mew, D.; Docktor, B.; Romano, C. Microwave Breast Imaging With a Monostatic Radar-Based System: A Study of Application to Patients. *IEEE Trans. Microw. Theory Tech.* **2013**, *61*, 2119–2128. [[CrossRef](#)]
10. Shere, M.; Lyburn, I.; Sidebottom, R.; Massey, H.; Gillett, C.; Jones, L. MARIA M5: A multicentre clinical study to evaluate the ability of the Micrima radio-wave radar breast imaging system (MARIA ) to detect lesions in the symptomatic breast. *Eur. J. Radiol.* **2019**, *116*, 61–67. [[CrossRef](#)]
11. Adachi, M.; Nakagawa, T.; Fujioka, T.; Mori, M.; Kubota, K.; Oda, G.; Kikkawa, T. Feasibility of portable microwave imaging device for breast cancer detection. *Diagnostics* **2021**, *12*, 27. [[CrossRef](#)]
12. Byrne, D.; O'Halloran, M.; Glavin, M.; Jones, E. Data independent radar beamforming algorithms for breast cancer detection. **2010**, *107*, 331–348. [[CrossRef](#)]
13. Fear, E.C.; Stuchly, M.A. Confocal microwave imaging for breast tumor detection: A study of resolution and detection ability. In Proceedings of the 2001 Conference Proceedings of the 23rd Annual International Conference of the IEEE Engineering in Medicine and Biology Society, Istanbul, Turkey, 25–28 October 2021.
14. Moein, M.; Ali, M.; Vijitha, P.; Manojit, P.; Mahdi, O. Eigenspace-Based Minimum Variance Combined with Delay Multiply and Sum Beamformer: Application to Linear-Array Photoacoustic Imaging. *IEEE J. Sel. Top. Quantum Electron.* **2018**, *25*, 1–8.
15. Mozaffarzadeh, M.; Yan, Y.; Mehrmohammadi, M.; Makkiabadi, B. Enhanced linear-array photoacoustic beamforming using modified coherence factor. *J. Biomed. Opt.* **2018**, *23*, 026005. [[CrossRef](#)] [[PubMed](#)]
16. Jeon, S.; Park, E.Y.; Choi, W.; Managuli, R.; Jong Lee, K.; Kim, C. Real-time delay-multiply-and-sum beamforming with coherence factor for in vivo clinical photoacoustic imaging of humans. *Photoacoustics* **2019**, *15*, 100136. [[CrossRef](#)] [[PubMed](#)]
17. Nilavalan, R.; Gbedemah, A.; Craddock, I.; Li, X.; Hagness, S.C. Numerical investigation of breast tumour detection using multi-static radar. *Electron. Lett.* **2003**, *39*, 1787–1789. [[CrossRef](#)]
18. Li, P.C.; Li, M.L. Adaptive imaging using the generalized coherence factor. *IEEE Trans. Ultrason. Ferroelectr. Freq. Control* **2003**, *50*, 128–141. [[PubMed](#)]
19. Hollman, K.; Rigby, K.; O'donnell, M. Coherence factor of speckle from a multi-row probe. In Proceedings of the 1999 IEEE Ultrasonics Symposium, Proceedings. International Symposium (Cat. No. 99CH37027), Tahoe, NV, USA, 17–20 October 1999; IEEE: New York, NY, USA, 1999; Volume 2, pp. 1257–1260.
20. Wang, S.L.; Chang, C.H.; Yang, H.C.; Chou, Y.H.; Li, P.C. Performance evaluation of coherence-based adaptive imaging using clinical breast data. *IEEE Trans. Ultrason. Ferroelectr. Freq. Control* **2007**, *54*, 1669–1679. [[CrossRef](#)]
21. Klemm, M.; Leendertz, J.; Gibbins, D.; Craddock, I.; Preece, A.; Benjamin, R. Microwave radar-based breast cancer detection: Imaging in inhomogeneous breast phantoms. *IEEE Antennas Wirel. Propag. Lett.* **2009**, *8*, 1349–1352. [[CrossRef](#)]
22. Zhang, Y.; Candra, P.; Wang, G.; Xia, T. 2-D entropy and short-time Fourier transform to leverage GPR data analysis efficiency. *IEEE Trans. Instrum. Meas.* **2014**, *64*, 103–111. [[CrossRef](#)]
23. Otsu, N. A threshold selection method from gray-level histograms. *IEEE Trans. Syst. Man Cybern.* **1979**, *9*, 62–66. [[CrossRef](#)]
24. Zhao, L. Motion track enhancement method of sports video image based on otsu algorithm. *Wirel. Commun. Mob. Comput.* **2022**, *2022*, 8354075. [[CrossRef](#)]
25. Zamani, A.; Abbosh, A. Hybrid clutter rejection technique for improved microwave head imaging. *IEEE Trans. Antennas Propag.* **2015**, *63*, 4921–4931. [[CrossRef](#)]
26. Elahi, M.A.; Glavin, M.; Jones, E.; O'Halloran, M. Artifact removal algorithms for microwave imaging of the breast. *Prog. Electromagn. Res.* **2013**, *141*, 185–200. [[CrossRef](#)]
27. Guo, L.; Abbosh, A.M. Optimization-based confocal microwave imaging in medical applications. *IEEE Trans. Antennas Propag.* **2015**, *63*, 3531–3539. [[CrossRef](#)]
28. Wang, J.; Zhang, M.; Bai, Y.; Xu, H.; Fan, Y. Distance compensation-based dual adaptive artifact removal algorithm in microwave breast tumor imaging system. *Biomed. Signal Process. Control* **2024**, *88*, 105598. [[CrossRef](#)]
29. Li, X.; Bond, E.J.; Van Veen, B.D.; Hagness, S.C. An overview of ultra-wideband microwave imaging via space-time beamforming for early-stage breast-cancer detection. *IEEE Antennas Propag. Mag.* **2005**, *47*, 19–34.
30. Kibria, S.; Samsuzzaman, M.; Islam, M.T.; Mahmud, M.Z.; Misran, N.; Islam, M.T. Breast phantom imaging using iteratively corrected coherence factor delay and sum. *IEEE Access* **2019**, *7*, 40822–40832. [[CrossRef](#)]
31. Shao, W.; McCollough, T. Advances in microwave near-field imaging: Prototypes, systems, and applications. *IEEE Microw. Mag.* **2020**, *21*, 94–119. [[CrossRef](#)]
32. Bai, Y.; Zhang, M.; Li, Z.; An, Q.; Hou, K.; Wang, J. The Vivaldi Antenna Design for Ultra-Wideband Biomedical Breast Imaging. In Proceedings of the 2023 IEEE 6th International Conference on Electronic Information and Communication Technology (ICEICT), Qingdao, China, 21–24 July 2023; IEEE: New York, NY, USA, 2023; pp. 309–312.

33. Arteaga-Marrero, N.; Villa, E.; González-Fernández, J.; Martín, Y.; Ruiz-Alzola, J. Polyvinyl alcohol cryogel phantoms of biological tissues for wideband operation at microwave frequencies. *PLoS ONE* **2019**, *14*, e0219997. [[CrossRef](#)]
34. Islam, M.T.; Samsuzzaman, M.; Kibria, S.; Islam, M.T. Experimental breast phantoms for estimation of breast tumor using microwave imaging systems. *IEEE Access* **2018**, *6*, 78587–78597. [[CrossRef](#)]
35. Özmen, V. Breast cancer in Turkey: Clinical and histopathological characteristics (analysis of 13.240 patients). *J. Breast Health* **2014**, *10*, 98. [[CrossRef](#)]
36. Klemm, M.; Craddock, I.; Leendertz, J.; Preece, A.; Gibbins, D.; Shere, M.; Benjamin, R. Clinical trials of a UWB imaging radar for breast cancer. In Proceedings of the Fourth European Conference on Antennas and Propagation, Barcelona, Spain, 12–16 April 2010; IEEE: New York, NY, USA, 2010; pp. 1–4.
37. Sultan, K.S.; Abbosh, A.M. Wearable dual polarized electromagnetic knee imaging system. *IEEE Trans. Biomed. Circuits Syst.* **2022**, *16*, 296–311. [[CrossRef](#)] [[PubMed](#)]
38. Khoshdel, V.; Asefi, M.; Ashraf, A.; LoVetri, J. Full 3D microwave breast imaging using a deep-learning technique. *J. Imaging* **2020**, *6*, 80. [[CrossRef](#)] [[PubMed](#)]
39. Bárbara, O.; Daniela, G.; Martin, O.; Martin, G.; Edward, J.; Raquel, C. Diagnosing Breast Cancer with Microwave Technology: Remaining Challenges and Potential Solutions with Machine Learning. *Diagnostics* **2018**, *8*, 36. [[CrossRef](#)]
40. Li, Y.; Xi, J.; Leung, C.K.W.; Li, T.; Tam, W.Y.; Li, J. Imaging by unsupervised feature learning of the wave equation. *Phys. Rev. Appl.* **2021**, *16*, 064039. [[CrossRef](#)]

**Disclaimer/Publisher’s Note:** The statements, opinions and data contained in all publications are solely those of the individual author(s) and contributor(s) and not of MDPI and/or the editor(s). MDPI and/or the editor(s) disclaim responsibility for any injury to people or property resulting from any ideas, methods, instructions or products referred to in the content.